The Astrophysical Journal, 854:56 (8pp), 2018 February 10 https://doi.org/10.3847/1538-4357/aaa769

ALMA Dust Polarization Observations of Two Young Edge-on Protostellar Disks

Chin-Fei Lee[1,2], Zhi-Yun Li[3], Tao-Chung Ching[4], Shih-Ping Lai[4], and Haifeng Yang[3]
[1] Academia Sinica Institute of Astronomy and Astrophysics, P.O. Box 23-141, Taipei 106, Taiwan; cflee@asiaa.sinica.edu.tw
[2] Graduate Institute of Astronomy and Astrophysics, National Taiwan University, No. 1, Sec. 4, Roosevelt Road, Taipei 10617, Taiwan
[3] Astronomy Department, University of Virginia, Charlottesville, VA 22904, USA
[4] Institute of Astronomy and Department of Physics, National Tsing Hua University, Hsinchu, Taiwan
Received 2017 December 1; revised 2017 December 31; accepted 2018 January 11; published 2018 February 12

Abstract

Polarized emission is detected in two young nearly edge-on protostellar disks in 343 GHz continuum at ∼50 au (∼0.″12) resolution with Atacama Large Millimeter/submillimeter Array. One disk is in HH 212 (Class 0) and the other in the HH 111 (early Class I) protostellar system. The polarization fraction is ∼1%. The disk in HH 212 has a radius of ∼60 au. The emission is mainly detected from the nearside of the disk. The polarization orientations are almost perpendicular to the disk major axis, consistent with either self-scattering or emission by grains aligned with a *poloidal* field around the outer edge of the disk because of the optical depth effect and temperature gradient; the presence of a poloidal field would facilitate the launching of a disk wind, for which there is already tentative evidence in the same source. The disk of HH 111 VLA 1 has a larger radius of ∼220 au and is thus more resolved. The polarization orientations are almost perpendicular to the disk major axis in the nearside, but more along the major axis in the farside, forming roughly half of an elliptical pattern there. It appears that toroidal and poloidal magnetic field may explain the polarization on the near and far sides of the disk, respectively. However, it is also possible that the polarization is due to self-scattering. In addition, alignment of dust grains by radiation flux may play a role in the farside. Our observations reveal a diversity of disk polarization patterns that should be taken into account in future modeling efforts.

Key words: accretion, accretion disks – ISM: individual objects (HH 111 and HH 212) – ISM: magnetic fields – polarization – stars: formation

1. Introduction

Stars generally form in magnetized molecular clouds. A fundamental problem of star formation in magnetized clouds is the so-called "magnetic flux problem." If all of the magnetic flux that threads a typical star-forming dense core is dragged into the central object, the stellar field strength would be orders of magnitude stronger than the observed value (Shu et al. 1987). How this longstanding puzzle is resolved is unclear. We aim to resolve this puzzle by detecting polarized emission with the Atacama Large Millimemeter/submillimeter Array (ALMA) from two nearly edge-on (with an inclination of 90° for edge-on) protostellar disks.

Specifically, we seek to determine whether some of the core magnetic flux is dragged into the disk or not. If yes, this flux would play a key role in both the disk evolution and the outflow launching. For disks that are non-self-gravitating, their evolution is believed to be driven by the magnetorotational instability (MRI, Balbus & Hawley 1991). However, in the weakly ionized outer parts of protostellar disks, the mass accretion rate driven by MRI is well below the observed level if the magnetic flux threading the disk is zero (e.g., Simon et al. 2013a). To be compatible with observations, there must be a net magnetic flux threading the outer parts of the disk (e.g., Simon et al. 2013b). Therefore, the averaged poloidal magnetic field on the disk must be non-zero. Similarly, in one of the two widely discussed scenarios of jet launching, the disk-wind picture (Konigl & Pudritz 2000, the other being the X-wind picture, Shu et al. 2000), a well-ordered poloidal magnetic field is required over an extended range of (inner) disk radii; the jet material is flung centrifugally to a high speed along the rapidly rotating poloidal field lines like "beads on a wire." Despite the fundamental role that the poloidal magnetic field plays in both the disk evolution and jet launching, it has never been firmly detected before.

The reason that the poloidal magnetic field has not been detected in disks to date through dust polarization is probably a combination of the resolution effect, source orientation, and evolutionary stage. Traditionally, dust polarization is used to infer the magnetic field morphology because the polarization can be produced by the alignment of (spinning) dust grains with their long axes perpendicular to the magnetic field (Andersson et al. 2015). However, recent observations found that dust polarization can also be produced by two other mechanisms: (1) self-scattering from dust grains of sizes comparable to the observed wavelength (Kataoka et al. 2015, 2016a; Yang et al. 2016a, 2016b), which is expected to be more significant in older disks where the dust grains have grown to submillimeter size, and (2) alignment of dust grains with their short axes along the direction of radiation anisotropy (Kataoka et al. 2017; Tazaki et al. 2017). Thus, the search of poloidal field becomes more complicated.

Polarization observations have been done in the dust continuum with the Submillimeter Array and the Combined Array for Research in Millimeter-wave Astronomy toward Class 0 sources, e.g., NGC 1333 4A (Girart et al. 2006), HH 211 (Lee et al. 2014), and a sample of others (Hull et al. 2014). In these sources, however, the disks remain unresolved (<100 au in diameter), and a polarization hole is seen, due to averaging of small-scale field structures in the disks. Once the disks are resolved, such as the Class 0 disks of IRAS 16293B and L1527, polarization can be detected. However, the IRAS 16293B disk is almost face-on, only the toroidal field can be detected (Rao et al. 2014). Although the L1527 disk is edge-on, it is unresolved in the vertical direction, which makes it difficult

to probe the detailed disk field structure (Segura-Cox et al. 2015). Polarization observations have also been done toward Class I sources. For the resolved disk, e.g., HL Tau (evolving from Class I to Class II phase), polarization is detected (Stephens et al. 2014, 2017; Kataoka et al. 2017). However, the published data are more consistent with the pattern from scattering by large grains and emission by radiative flux-aligned grains rather than from emission by magnetically aligned grains (Kataoka et al. 2016a; Yang et al. 2016b; Stephens et al. 2017). Polarization observations have also been done toward Class II sources, but the polarization was found to arise mainly from self-scattering by large grains (Kataoka et al. 2016b). Large grains are expected in relatively evolved sources that have a longer time for the grains to grow compared to the youngest protostars. In addition, self-scattering can also contribute significantly to the polarization in disks around massive stars (Fernández-López et al. 2016).

As discussed above, to have the best chance of detecting the poloidal magnetic field, the disks must be (1) resolved, (2) close to edge-on to avoid depolarization due to the poloidal field at a small inclination angle, and (3) as young as possible to reduce the chance of polarization contamination from scattering, since there would be less time for the grains to grow to large enough sizes for efficient scattering. These criteria are satisfied by two bright nearby disks in Orion at a distance of ∼400 pc, one in HH 212 (Class 0) and one in HH 111 (early Class I). Moreover, highly collimated jets (Reipurth et al. 1999; Lee et al. 2017a) are seen launching from them, indicating that the disks should have a poloidal field at least in the inner part. In addition, our ALMA data in molecular lines have resolved the disks and found them to have a Keplerian rotation (Lee et al. 2016, 2017d). In this paper, we present our polarization observations toward these two disks to search for the poloidal field.

2. Observations

Polarization observations toward the HH 111 and HH 212 protostellar systems were carried out together with ALMA in Band 7 at ∼343 GHz in Cycle 3, with 38–40 antennas in the Configuration C36-6. Two executions were carried out in 2016, one on August 30 and the other on September 3. The projected baselines are 14–2483 m. The maximum recoverable size scale is ∼1.″4, enough to cover the disks seen in the continuum. One pointing was used to map the center of the system. The correlator was set up to have four continuum windows (with one at 336.5 GHz, one at 338.5 GHz, one at 348.5 GHz, and one at 350.5 GHz), with a central frequency at ∼343 GHz. The total time is ∼40 minutes on each HH system.

The *uv* data were calibrated with the Common Astronomy Software Applications package, with quasars J5010+1800, J0552+0313 (0.31 Jy), and J0522–3627 (3.04 Jy) as bandpass, gain, and polarization calibrators, respectively. A super-uniform weighting with a robust factor of 0.5 was used for the *uv* data to generate the continuum maps of the disks at ∼343 GHz. Notice that the *uv* data with a distance < 50 m are not well sampled and thus excluded in our map generation. This generates a synthesized beam (resolution) of ∼0.″12. In Stokes *I* maps, the noise level is ∼0.44 mJy beam^{-1} in HH 212 and ∼0.34 mJy beam^{-1} in HH 111. In Stokes *Q* and *U* maps, the noise is ∼0.03 mJy beam^{-1} in both sources. The (linear) polarization fraction (degree) is defined as $P = \sqrt{Q^2 + U^2}/I$. According to the ALMA Technical Handbook in Cycle 5, the instrumental error on *P* is expected to be $\lesssim$0.2% for the disks of HH 212 and HH 111 VLA 1 at the phase center, because their disk size is $\lesssim$1″ and thus much smaller than 1/3 of the primary beam, which is ∼17″. It could increase to ∼0.3% for the disk of HH 111 VLA 2, which is located at ∼3″ away from the VLA 1 source. Polarization orientations are defined by the *E* vectors.

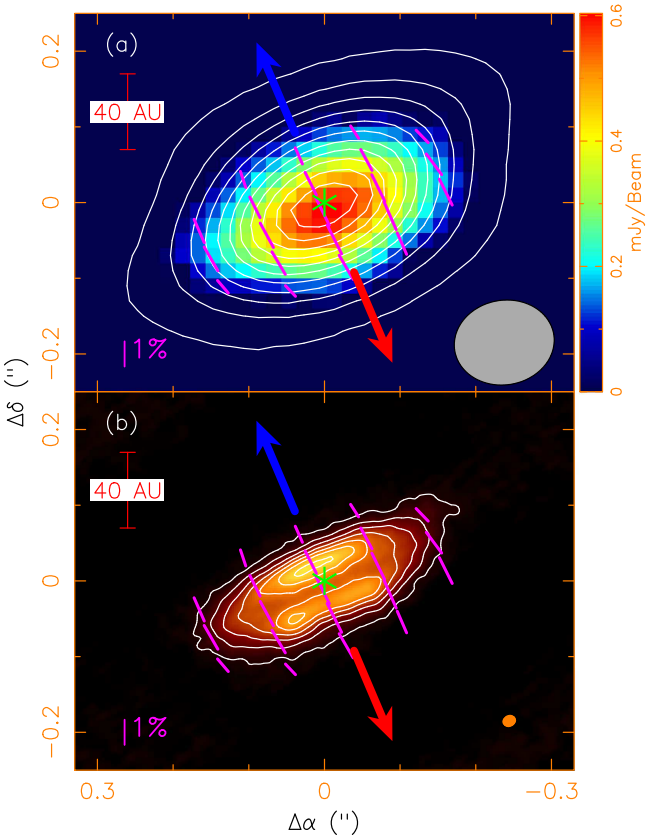

Figure 1. HH 212. (a) The continuum map (white contours) toward the central source (asterisk) at 343 GHz at ∼0.″12 resolution, with the polarized intensity map (color map) and polarization orientations (line segments). The blue and red arrows show the approaching and receding sides of the jet axis, respectively. The contours start at 6σ with a step of 10σ, where σ = 0.44 mJy beam^{-1}. (b) The same polarization orientations on the continuum map of the dusty disk (orange map with white contours) obtained before at 0.″02 resolution (see Figure 1(d) in Lee et al. 2017c). The disk on the side of the redshifted jet is the nearside.

3. Results

3.1. HH 212

Figure 1(a) shows the continuum map (white contours) toward the central source in HH 212 at 343 GHz at ∼0.″12 resolution, with the polarized intensity map (color map) and polarization orientations (line segments). The continuum map shows an elongated structure perpendicular to the jet axis. The total flux density is ∼150 ± 25 mJy. As seen in Figure 1(b), the continuum emission within ∼0.″2 of the central source is spatially coincident with the dusty disk (orange map with white contours) detected before at 350 GHz at ∼0.″02 resolution (Lee et al. 2017c) and thus mainly traces the dusty disk around the central source. According to that paper, the disk is nearly edge-on, with an inclination of ∼86° and the nearside tilted slightly to the south. In addition, the disk is flared with a dark lane along the equatorial plane. However, the disk here is mainly

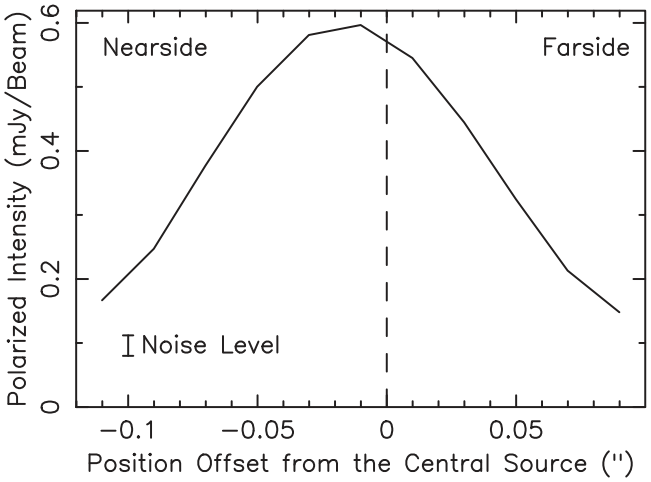

Figure 2. HH 212—Polarized intensity along the minor axis of the disk.

resolved in the major axis and only marginally resolved in the minor axis along the vertical direction.

Polarized emission is detected toward the dusty disk, with a polarization fraction of ∼1%, as indicated by the length of the line segments. The polarized intensity increases toward the center. It is slightly higher below the major axis of the disk than above, producing a near-far side asymmetry in the polarized intensity. This asymmetry is significant because the polarized intensity in the nearside peaks at approximately −0.″014 (from Gaussian fit) with a value higher than that at 0.″014 on the farside by more than a noise level, as shown in Figure 2. The polarization orientations are all roughly perpendicular to the major axis of the disk.

3.2. HH 111

In HH 111, there are two sources, VLA 1 and VLA 2, with VLA 1 being the source driving the HH 111 jet. Figure 3(a) shows the continuum map (white contours) toward the VLA 1 source at 343 GHz at ∼0.″12 resolution, with the polarized intensity map (color map) and polarization orientations (line segments). A dusty disk has been detected before in continuum at 230 GHz at up to ∼0.″35 resolution (Lee 2010, 2011; Lee et al. 2016). It is also close to edge-on, but with a smaller inclination angle of ∼80° and the nearside tilted to the east (Lee et al. 2016). This dusty disk is now better resolved at higher resolution obtained at higher frequency. It appears to be exactly perpendicular to the jet axis, with a Gaussian deconvolved size of ∼0.″54 in the major axis and ∼0.″18 in the minor axis. It has a total flux density of ∼535 ± 80 mJy. Previously with the $C^{18}O$ $J = 2$–1 line emission, the disk was found to have a Keplerian rotation within a radius of ∼0.″4 of the central source (Lee et al. 2016), and this radius is roughly coincident with the edge of the disk detected here.

Polarized emission is detected toward the disk, with a polarization fraction of ∼1%. As found in HH 212, the polarized intensity increases toward the center. Since the disk is better resolved in the minor axis because of its lower inclination angle and larger disk radius, the emission in the nearside and farside can be better separated. As can be seen, the polarized intensity is much higher in the nearside of the disk than the farside. Interestingly, the polarization orientations are mainly perpendicular to the major axis of the disk in the nearside, but bended around the jet axis in the farside, forming the upper half of an elliptical polarization pattern. As a result, a polarization gap is seen right above the major axis, with less polarization closer to the jet axis, due to the depolarization of orthogonal polarizations there.

Figure 3(b) shows the continuum map (white contours) toward the VLA 2 source at 343 GHz at ∼0.″12 resolution, with the polarized intensity map (color map) and polarization orientations (line segments). The VLA 2 source is located at ∼3″ (1200 au) to the northwest of the VLA 1 source. Its continuum emission structure is slightly elongated at a position angle of ∼117°, with a Gaussian deconvolved size of ∼0.″068, and thus can have a major axis at this position angle. The VLA 2 source could be driving the HH 121 jet (Sewiło et al. 2017), because its major axis is roughly perpendicular to the jet, which has a position angle of ∼30° ± 15° (as roughly indicated by the blue and red arrows). As a result, the continuum emission may trace a flattened dusty envelope or a small dusty disk around the VLA 2 source. It has a total flux density of ∼18.2 ± 3.6 mJy. The polarization orientations are perpendicular to the major axis of the continuum emission, like that seen in HH 212.

4. A Disk Model for HH 111

Disk properties are needed to understand the dust polarization and then to study if the dust polarization can be used to infer the magnetic field morphology in the disk. Since the disk properties of HH 212 have already been determined by Lee et al. (2017c), we only aim to determine the disk properties of HH 111 around the VLA 1 source. Previously, a simple flat disk model was adopted for simplicity to model the disk emission in continuum at 230 GHz at ∼0.″35 resolution (Lee 2011). Since the disk is roughly resolved here in the minor axis, we adopt a flared disk model similar to that used before to model the disk emission in HH 212 at higher resolution (Lee et al. 2017c). Notice that, without having observations in more than one frequency at higher angular resolution, we are not able to constrain the physical properties of the disk accurately. Thus, the model here is really for illustrative purposes only.

As in Lee et al. (2017c), we introduce a parametrized model for the disk emission, in order to roughly obtain the properties of the disk. For a disk in vertical hydrostatic equilibrium, the scale height h in the cylindrical coordinate system is given by

$$\frac{h}{R} \sim \frac{c_s}{v_\phi} \propto \frac{R^{-q/2}}{R^{-1/2}} = \left(\frac{R}{R_o}\right)^{(1-q)/2}, \quad (1)$$

where R is the cylindrical radius and c_s is the isothermal sound speed proportional to $T^{1/2}$, where T is the temperature. Assuming $T \propto R^{-q}$, we have $c_s \propto R^{-q/2}$. v_ϕ is the rotational velocity assumed to be Keplerian and thus is proportional to $R^{-1/2}$, as suggested by $C^{18}O$ gas kinematics (Lee et al. 2016). In this case, the scale height of the disk increases with the disk radius monotonically. However, Figure 3(a) shows that the continuum emission of the disk becomes geometrically thinner near the outer edge, as seen in HH 212 (Lee et al. 2017c). The physical reason for the behavior is unclear; self-shielding could reduce the temperature in the outer part of the disk and thus the disk scale height (Dullemond & Dominik 2004). To model the decrease of disk thickness near the outer edge, we introduce a radius, R_t, beyond which the scale height decreases to zero at

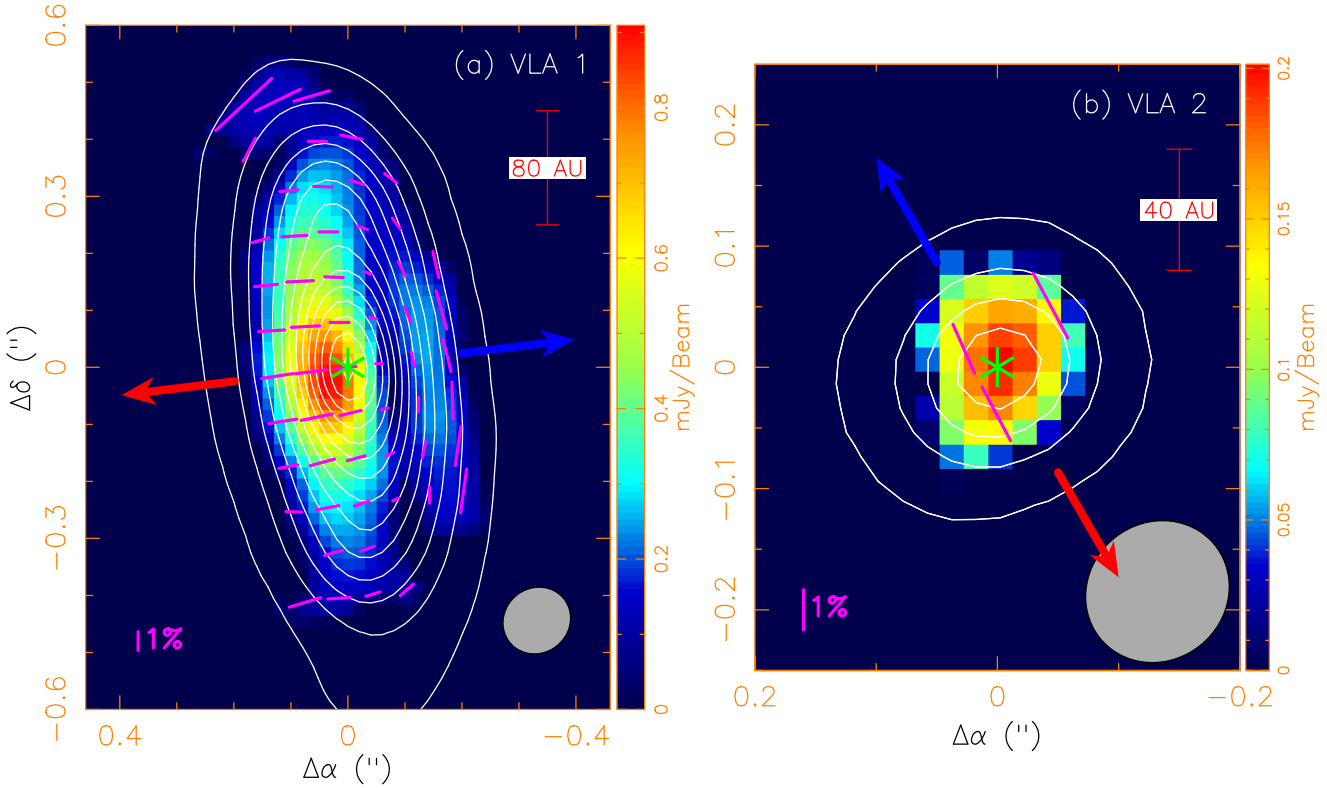

Figure 3. HH 111. (a) The continuum map (white contours) toward the VLA 1 source (asterisk) at 343 GHz at ∼0.″12 resolution, with the polarized intensity map (color map) and polarization orientations (line segments). The blue and red arrows show the approaching and receding sides of the jet axis, respectively. The contours start at 6σ with a step of 15σ, where $\sigma = 0.34$ mJy beam^{-1}. (b) Same as (a) but toward the VLA 2 source (asterisk). The blue and red arrows show roughly the mean orientation of the HH 121 jet, which has a position angle of 30° ± 15° (Sewiło et al. 2017). The contours start at 4σ with a step of 10σ, where $\sigma = 0.34$ mJy beam^{-1}. The disk on the side of the redshifted jet is the nearside.

the outer radius of the disk R_o. Let h_t be the scale height of the disk at R_t, we have

$$h(R) \sim h_t \begin{cases} \left(\frac{R}{R_t}\right)^{1+(1-q)/2} & \text{if } R < R_t, \\ \sqrt{1-\left(\frac{R-R_t}{R_o-R_t}\right)^2} & \text{if } R_t \leqslant R \leqslant R_o \end{cases}. \quad (2)$$

The temperature is simply assumed to increase radially toward the center with

$$T \sim T_t \left(\frac{R}{R_t}\right)^{-q}, \quad (3)$$

where T_t is the temperature at R_t and q is the power-law index. The number density of molecular hydrogen is assumed to be

$$n = n_t \left(\frac{R}{R_t}\right)^{-p} \exp\left(-\frac{z^2}{2h^2}\right), \quad (4)$$

where p is the power-law index and n_t is the number density in the disk midplane at R_t. Here the density is assumed to decrease exponentially above the disk midplane. Helium is included so that the mass density is $\rho = 1.4 n m_{H_2}$.

Dust opacity is needed to derive the dust emission. For the circumstellar disk, the dust opacity formula can be given as

$$\kappa_\nu = 0.1 \left(\frac{\nu}{10^{12}\text{Hz}}\right)^\beta \text{ cm}^2 \text{ g}^{-1}, \quad (5)$$

where β is the dust opacity spectral index (Beckwith et al. 1990). Based on the SED (spectral energy distribution) fitting to the continuum flux around the central source obtained at much lower resolution of a few arcseconds, β was found to be ∼0.9 (Lee et al. 2009). At that low resolution, the flux comes from both the disk and envelope. Since the disk itself is expected to have a lower β due to a larger grain size, we assume $\beta \sim 0.6$, such as that found in the disk of HH 212 (Lee et al. 2008). Thus, the dust opacity is $\kappa_\nu \sim 0.053$ cm^2 g^{-1} at 343 GHz. Note that the value of β only affects the required mass of the disk to produce the observed emission. Smaller β implies larger κ_ν, and thus lower disk mass.

We used our radiative transfer code (Lee et al. 2017c) to obtain dust continuum emission map from the model disk. We first computed the thermal emission from each point in the disk based on its local temperature, and then generated a synthetic map by integrating along each line of sight the local emission that is attenuated by the optical depth. The disk is assumed to have an inclination angle of ∼80°. The resulting map is then convolved with the observed beam in order to generate a model map to be compared with the observed map at the same resolution.

Since HH 111 is a Class I source, we assume $q = 0.5$, as that found for the disk in the later stage (Andrews et al. 2009). We also assume $p = 1$ and use an eye-fitting for the rough determination of the disk properties. The best-fit parameters are $R_o \sim 0.''55 \pm 0.''11$ (220 ± 44 au), $R_t \sim 0.''15 \pm 0.''03$ (60 ± 12 au), $h_t \sim 0.''08 \pm 0.''02$ (32 ± 8 au), $n_t \sim 1.3 \pm 0.3 \times 10^9$ cm^{-3}, and $T_t \sim 87 \pm 17$ K. Note that the best-fit

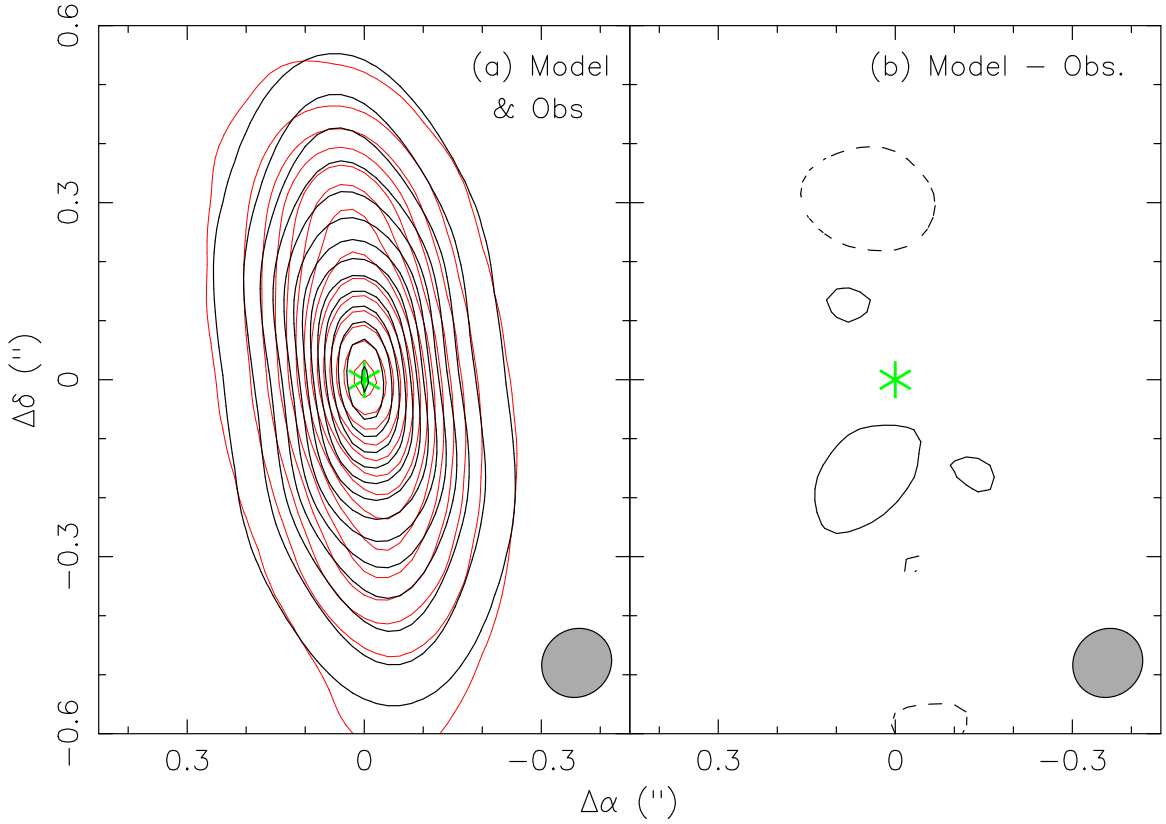

Figure 4. Modeling of the HH 111 VLA 1 disk. (a) Model disk emission map (black contours) on top of the observed map (red contours). (b) Residual (Model-Observation). In both panels, the contours start at the same level with the same step as in Figure 3(a).

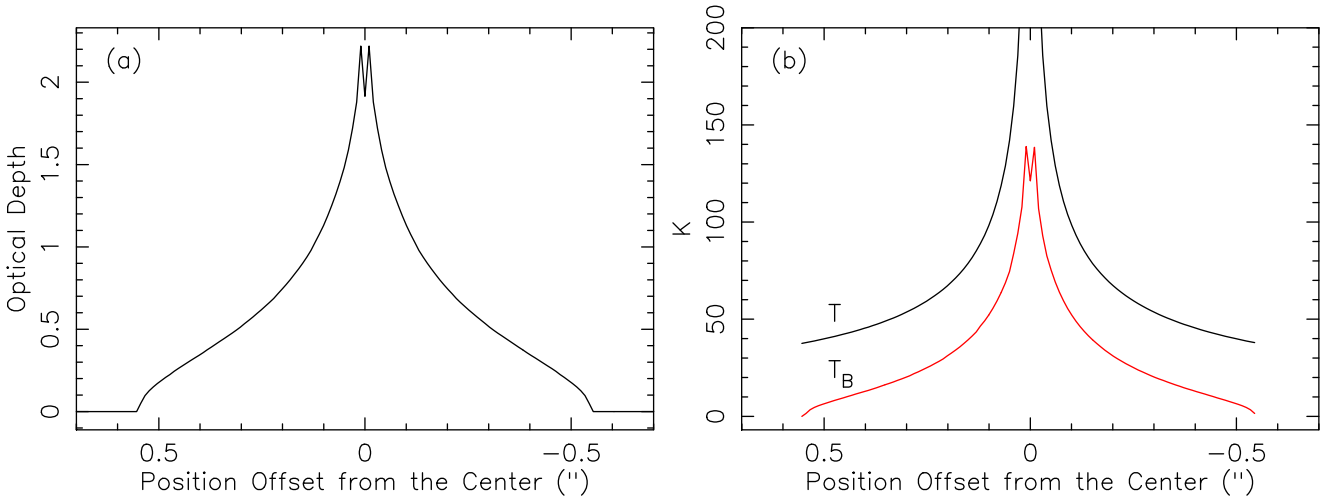

Figure 5. Optical depth and brightness temperature in our model for the HH 111 VLA 1 disk along the disk major axis. Panel (a) shows the optical depth. Panel (b) shows the brightness temperature (red) in comparison to the temperature (black) in the model.

parameters are assumed to have 20% uncertainties. Since $R_t \sim 0.27R_o$, most part of the disk (with a radius $>R_t$) is almost flat with roughly a constant thickness. With $p = 1$, the surface density of the disk is roughly proportional to r^{-1} for most of the disk, similar to that found before in Lee (2011) for the HH 111 disk emission at a lower resolution and in older disks (Andrews et al. 2009). Figures 4(a) and (b) show the best-fit model disk map on top of the observed map and the residual, respectively. The residual is reasonably small, indicating that the disk model is acceptable. In this model, the dust emission is optically thin except for the innermost 0.″2 region, and thus the brightness temperature (before convolved with the observed beam) is much lower than $(1 - e^{-\tau})$ times the temperature, as shown in Figure 5.

At $R = R_t$, the Keplerian rotation velocity is $v_\phi \sim 4.5$ km s^{-1} (Lee et al. 2016). The midplane temperature there is ~87 K, yielding an isothermal speed of ~0.6 km s^{-1}. Thus, the scale height at R_t is expected to be ~8 au, which is much smaller than the value of h_t inferred from the continuum modeling. Thus, the scale height could be overestimated. Radiation heating by the central protostar could help increase the scale height but more detailed modeling is needed to

quantify this effect. In any case, higher resolution observation to better resolve the vertical structure is needed to confirm the disk structure. In this model, the disk has a total mass of

$$M_D = 1.4\, m_{\rm H_2} \int n\, 2\pi\, R\, dR\, dz \sim 0.04\, M_\odot, \quad (6)$$

which is approximately only 2%–3% of the mass (1.3–1.8 $M_\odot$; Lee et al. 2016) of the central protostar, supporting the fact that the disk can indeed rotate with a Keplerian velocity. Again, since our model is based on the observation in one single frequency, the model results here should be used with caution.

5. Discussion

As mentioned in the Introduction, three mechanisms can produce the polarization in dust emission at (sub)millimeter wavelengths:

(1) Alignment of (spinning) dust grains with their long axes perpendicular to the magnetic field (Andersson et al. 2015), as seen in the envelope in NGC 1333 IRAS 4A (Girart et al. 2006) and probably in the disk in IRAS 16293-2422 B (Rao et al. 2014). In the envelope and disk, the temperature is expected to increase toward the center. In the optically thin case, the polarization orientations will be perpendicular to the magnetic field direction, because the emission with the polarization orientation parallel to the magnetic field direction has a smaller opacity. However, in the optically thick case, the polarization orientations will be parallel to the magnetic field direction, because the emission with the polarization orientation parallel to the magnetic field direction can probe deeper in the envelope and disk where the temperature (and thus the source function for emission) is higher. Readers can refer to Section 2.2 in Yang et al. (2017) for a more detailed discussion.

(2) Self-scattering from dust grains of sizes comparable to the observed wavelength (Kataoka et al. 2015, 2016a; Yang et al. 2016a, 2016b), as seen in the evolved disk in HL Tau, especially in ALMA Band 7 (0.87 mm; Stephens et al. 2017). The self-scattering can be efficient in submillimeter wavelengths when the grains have grown to bigger than $\sim$100 μm (Kataoka et al. 2015; Yang et al. 2017). For an inclined disk, it can produce a near-far side asymmetry in polarized intensity and polarization orientations perpendicular to the major axis (Yang et al. 2017). This is because the near-side of the disk surface is viewed more edge-on than the far-side. Larger grains and higher density will produce larger near-far side asymmetry (Yang et al. 2017).

(3) Alignment of dust grains with their short axes along the direction of radiation flux (anisotropy; Kataoka et al. 2017; Tazaki et al. 2017), as proposed for the observed dust polarization detected in the evolved disk in HL Tau at 3 mm (Kataoka et al. 2017). In the disk, the radiation flux is expected to be radially directed, and thus the dust grains can be aligned with their short axes in the radial direction. As a result, the polarization orientation would be circular around the central source for a face-on disk, elliptical for an inclined disk, and mostly parallel to the major axis for a nearly edge-on disk.

In the following, we discuss our observations in the context of these mechanisms.

5.1. HH 212

In HH 212, the emission is mainly from the nearside of the disk, because of the high inclination angle, large geometric thickness, and high optical depth of the disk (Lee et al. 2017c). In addition, the emission detected here is mainly from the outer edge of the disk because the emission there has become optically thick. Although the disk is young in the Class 0 phase, the grain size in the outer edge of the disk may have grown quickly to the submillimeter size (Brauer et al. 2008). However, since the disk dust emission is observed to be vertically extended, the grain settling is unlikely to have taken place significantly. Hence, the grains are likely relatively small, although detailed modeling is required to constrain the grain size quantitatively.

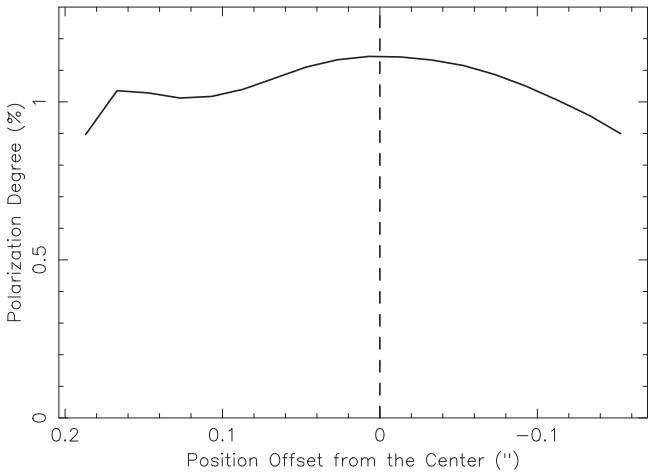

Figure 6. Profile of the polarization degree along the major axis of the HH 212 disk, averaged with a width of 0.″08 perpendicular to the major axis.

It is possible that the observed dust polarization is due to magnetic alignment of the dust grains. In HH 212, the temperature of the disk increases toward the center (Lee et al. 2017c). Since the emission has become optically thick in the outer edge of the disk, the inferred magnetic field lines would be parallel to polarization orientations and thus be mainly poloidal. The lack of variation in polarization degree from the center to the disk edges (Figure 6) strengthens the possibility for the optically thick case somewhat, although the rather low resolution makes it inconclusive in our view. If this is the case, the magnetic fields may be responsible for launching the rotating SO/SO_2 outflow extending out from the disk (Lee et al. 2017b; Tabone et al. 2017). Observations at higher resolution are needed to determine the location of the magnetic fields more accurately.

Since the grains may have grown to submillimeter size, it is also possible that the observed dust polarization be due to self-scattering (Kataoka et al. 2015). For an inclined disk, the self-scattering tends to produce polarization along the minor axis of the projected disk (Kataoka et al. 2016a; Yang et al. 2016b), which is in qualitative agreement with the pattern observed in HH 212. In addition, for an optically thick disk such as HH 212, the near-side of the disk is expected to be brighter in polarized intensity than the far-side, which is also observed. However, whether scattering can reproduce the observations quantitatively or not remains to be determined. We will postpone a detailed modeling to a future investigation.

The observed dust polarization is unlikely to be due to the alignment of dust grains by the radiation flux, because the polarization orientations are observed to be perpendicular to the major axis, which is opposite to the expected (parallel to the major axis) pattern.

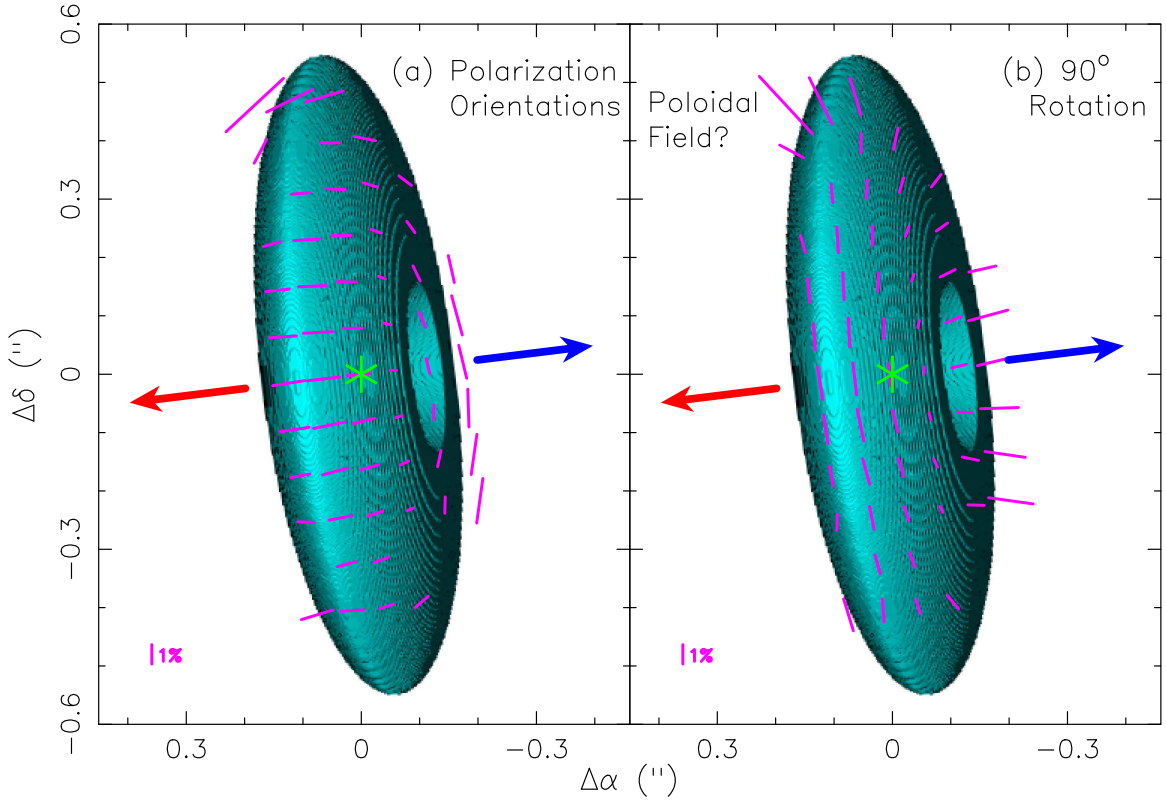

Figure 7. HH 111 VLA 1. (a) Polarization orientations plotted on the model disk structure, which shows the scale height of the disk times a factor $\sqrt{2}$. (b) Possible magnetic field orientations, inferred by rotating the polarization orientations by 90°, plotted on the model disk structure.

5.2. HH 111

In HH 111, the disk around the VLA 1 source is more evolved than that in HH 212. According to our simple model, it has a larger radius of ∼220 au (0.″55) and a lower inclination angle of ∼80°, and thus the emission from the nearside and farside of the disk can be better separated. Interestingly, the polarization orientations are different between the nearside and farside. The polarized intensity shows a larger near-far side asymmetry than that seen in HH 212.

Like HH 212, it is possible that the observed dust polarization of the VLA 1 disk is due to magnetic alignment of the dust grains. Since the disk has a temperature increasing toward the center and is mostly optically thin as discussed in Section 4, the inferred magnetic field orientations could be obtained by rotating the polarization orientations by 90°. Hence, the magnetic field in the nearside could be mainly toroidal in the disk (see Figure 7), as expected for a well ionized disk where the magnetic field is expected to be wound onto a predominantly toroidal configuration by differential rotation. Near the northern edge of the disk, the field lines appear to be poloidal and thus could trace the poloidal fields dragged into the disk from the innermost envelope (see Figure 7(b)); HH 111 is a source where we have previously uncovered evidence for a decrease of specific angular momentum in the envelope-disk transition region, from the 1000 to 100 au scale, which is indicative of magnetic braking (Lee et al. 2016). It is therefore not too surprising if magnetic fields exist in the disk as well. In the farside of the disk above the major axis, the field lines appear to be parallel to the jet axis, and thus could trace poloidal fields extending out from the inner part of the disk. As in the HH212 case, the inferred poloidal field may also be related to the large-scale, ordered, magnetic field that is commonly invoked for outflow driving. However, the polarization pattern there can also be considered as half of an elliptical pattern, and thus be due to the dust alignment by the radiation flux in the disk (Kataoka et al. 2017; Tazaki et al. 2017).

It is also possible that the observed dust polarization is due to self-scattering by dust grains. The self-scattering can produce a near-far side asymmetry in polarized intensity for an inclined disk reminiscent of that observed in HH 111. In the nearside of the disk, the observed polarization orientations are perpendicular to the major axis, as seen in the self-scattering model (Yang et al. 2017). In the farside of the disk, however, the observed polarization orientations are parallel to the major axis, which is not seen in the self-scattering models where the disk is not viewed as nearly edge-on (Yang et al. 2017). It is possible that the disk has prominent rings and gaps, as seen in HL Tau. For such a disk, Pohl et al. (2016) found that the polarization orientations due to self-scattering can be parallel to the major axis, if the disk is edge-on and optically thin. It is plausible that a more optically thick disk with rings and gaps that is inclined slightly away from edge-on may produce a polarization pattern similar to that observed in HH 111 (perpendicular to the major axis on the nearside and parallel to it on the farside). Further observations at higher resolution and modeling are needed to check this possibility.

It is more uncertain to discuss the polarization for the dust emission around the VLA 2 source because its structure and physical properties are poorly constrained due to insufficient resolution. As discussed earlier, the VLA 2 source could be driving the HH 121 jet and the continuum emission could trace a flattened dusty envelope or a small dusty disk perpendicular to the jet. Assuming that the emission is optically thin, $\beta \sim 1$, and the temperature is ∼50 K, the mass for the dust emission is only ∼2 Jupiter mass. The polarization along the apparent

minor axis of the disk may be due to a toroidal field (if optically thin) or self-scattering.

6. Conclusions

Dust polarization has been detected toward two nearly edge-on protostellar disks. The interpretation of the polarization is complicated by the presence of three different polarization mechanisms. In HH 212, the dust polarization is consistent with either scattering or emission by grains aligned with a *poloidal* field around the outer edge of the disk because of the optical depth effect and temperature gradient. One may be able to tell these two apart with polarization observations at another wavelength in the future. For HH 111 VLA 1, it is possible that a combination of toroidal and poloidal magnetic fields may explain the polarization on the near and far sides of the disk, although we do not have good detailed models for scattering for disks that are as edge-on as HH 111; scattering may or may not work, and it needs more exploration. In addition, alignment of dust grains by radiation flux may play a role in the farside. Perhaps, different polarization mechanisms are operating in different parts of a disk and in different disks. Additional multi-wavelength polarization observations and detailed modeling are required to make further progress in this important field that is being revolutionized by ALMA.

We thank the anonymous referee for useful comments. C.-F.L. thanks A. Kataoka and T. Hoang for fruitful discussion. This paper makes use of the following ALMA data: ADS/JAO. ALMA# 2015.1.00037.S ALMA is a partnership of ESO (representing its member states), NSF (USA) and NINS (Japan), together with NRC (Canada), MoST and ASIAA (Taiwan), and KASI (Republic of Korea), in cooperation with the Republic of Chile. The Joint ALMA Observatory is operated by ESO, AUI/NRAO, and NAOJ. C.-F.L. acknowledges grants from the Ministry of Science and Technology of Taiwan (MoST 104-2119-M-001-015-MY3) and the Academia Sinica (Career Development Award). Z.Y.L. is supported in part by NASA NNX14AB38G and NSF AST-1313083 and 1716259.

ORCID iDs

Chin-Fei Lee https://orcid.org/0000-0002-3024-5864
Shih-Ping Lai https://orcid.org/0000-0001-5522-486X

References

Andersson, B.-G., Lazarian, A., & Vaillancourt, J. E. 2015, ARA&A, 53, 501
Andrews, S. M., Wilner, D. J., Hughes, A. M., Qi, C., & Dullemond, C. P. 2009, ApJ, 700, 1502
Balbus, S. A., & Hawley, J. F. 1991, ApJ, 376, 214
Beckwith, S. V. W., Sargent, A. I., Chini, R. S., & Guesten, R. 1990, AJ, 99, 924
Brauer, F., Dullemond, C. P., & Henning, T. 2008, A&A, 480, 859
Dullemond, C. P., & Dominik, C. 2004, A&A, 417, 159
Fernández-López, M., Stephens, I. W., Girart, J. M., et al. 2016, ApJ, 832, 200
Girart, J. M., Rao, R., & Marrone, D. P. 2006, Sci, 313, 812
Hull, C. L. H., Plambeck, R. L., Kwon, W., et al. 2014, ApJS, 213, 13
Kataoka, A., Muto, T., Momose, M., et al. 2015, ApJ, 809, 78
Kataoka, A., Muto, T., Momose, M., Tsukagoshi, T., & Dullemond, C. P. 2016a, ApJ, 820, 54
Kataoka, A., Tsukagoshi, T., Momose, M., et al. 2016b, ApJL, 831, L12
Kataoka, A., Tsukagoshi, T., Pohl, A., et al. 2017, ApJL, 844, L5
Konigl, A., & Pudritz, R. E. 2000, in Protostars and Planets IV, ed. V. Manning, A. P. Boss, & S. S. Russell (Tucson, AZ: Univ. Arizona Press), 759
Lee, C.-F. 2010, ApJ, 725, 712
Lee, C.-F. 2011, ApJ, 741, 62
Lee, C.-F., Ho, P. T. P., Bourke, T. L., et al. 2008, ApJ, 685, 1026
Lee, C.-F., Ho, P. T. P., Li, Z.-Y., et al. 2017a, NatAs, 1, 0152
Lee, C.-F., Hwang, H.-C., & Li, Z.-Y. 2016, ApJ, 826, 213
Lee, C.-F., Li, Z.-Y., Codella, C., et al. 2017b, ApJ, submitted
Lee, C.-F., Li, Z.-Y., Ho, P. T. P., et al. 2017c, SciA, 3, e1602935
Lee, C.-F., Li, Z.-Y., Ho, P. T. P., et al. 2017d, ApJ, 843, 27
Lee, C.-F., Mao, Y.-Y., & Reipurth, B. 2009, ApJ, 694, 1395
Lee, C.-F., Rao, R., Ching, T.-C., et al. 2014, ApJL, 797, L9
Pohl, A., Kataoka, A., Pinilla, P., et al. 2016, A&A, 593, A12
Rao, R., Girart, J. M., Lai, S.-P., & Marrone, D. P. 2014, ApJL, 780, L6
Reipurth, B., Yu, K., Rodriguez, L. F., Heathcote, S., & Bally, J. 1999, A&A, 352, L83
Segura-Cox, D. M., Looney, L. W., Stephens, I. W., et al. 2015, ApJL, 798, L2
Sewiło, M., Wiseman, J., Indebetouw, R., et al. 2017, ApJ, 849, 68
Shu, F. H., Adams, F. C., & Lizano, S. 1987, ARA&A, 25, 23
Shu, F. H., Najita, J. R., Shang, H., & Li, Z.-Y. 2000, in Protostars and Planets IV, ed. V. Manning, A. P. Boss, & S. S. Russell (Tucson, AZ: Univ. Arizona Press), 789
Simon, J. B., Bai, X.-N., Armitage, P. J., et al. 2013, ApJ, 764, 66
Simon, J. B., Bai, X.-N., Armitage, P. J., et al. 2013, ApJ, 775, 73
Stephens, I. W., Looney, L. W., Kwon, W., et al. 2014, Natur, 514, 597
Stephens, I. W., Yang, H., Li, Z.-Y., et al. 2017, ApJ, 851, 55
Tabone, B., Cabrit, S., Bianchi, E., et al. 2017, A&A, 607, L6
Tazaki, R., Lazarian, A., & Nomura, H. 2017, ApJ, 839, 56
Yang, H., Li, Z.-Y., Looney, L., & Stephens, I. 2016a, MNRAS, 456, 2794
Yang, H., Li, Z.-Y., Looney, L. W., et al. 2016b, MNRAS, 460, 4109
Yang, H., Li, Z.-Y., Looney, L. W., Girart, J. M., & Stephens, I. W. 2017, MNRAS, 472, 373